IOP PUBLISHING PHYSICS IN MEDICINE AND BIOLOGY

Phys. Med. Biol. **56** (2011) 6475–6493 doi:10.1088/0031-9155/56/19/019

A combined molecular dynamics and Monte Carlo simulation of the spatial distribution of energy deposition by proton beams in liquid water

Rafael Garcia-Molina[1], Isabel Abril[2], Santiago Heredia-Avalos[3], Ioanna Kyriakou[4] and Dimitris Emfietzoglou[4]

[1] Departamento de Física, Centro de Investigación en Óptica y Nanofísica (CIOyN), Universidad de Murcia, E-30100 Murcia, Spain
[2] Departament de Física Aplicada, Universitat d'Alacant, E-03080 Alacant, Spain
[3] Departament de Física, Enginyeria de Sistemes i Teoria del Senyal, Universitat d'Alacant, E-03080 Alacant, Spain
[4] Medical Physics Laboratory, University of Ioannina Medical School, GR-45110 Ioannina, Greece

E-mail: rgm@um.es

Received 16 June 2011, in final form 2 August 2011
Published 20 September 2011
Online at stacks.iop.org/PMB/56/6475

Abstract

We have evaluated the spatial distribution of energy deposition by proton beams in liquid water using the simulation code SEICS (Simulation of Energetic Ions and Clusters through Solids), which combines molecular dynamics and Monte Carlo techniques and includes the main interaction phenomena between the projectile and the target constituents: (i) the electronic stopping force due to energy loss to target electronic excitations, including fluctuations due to the energy-loss straggling, (ii) the elastic scattering with the target nuclei, with their corresponding energy loss and (iii) the dynamical changes in projectile charge state due to electronic capture and loss processes. An important feature of SEICS is the accurate account of the excitation spectrum of liquid water, based on a consistent *solid-state* description of its energy-loss-function over the whole energy and momentum space. We analyse how the above-mentioned interactions affect the depth distribution of the energy delivered in liquid water by proton beams with incident energies of the order of several MeV. Our simulations show that the position of the Bragg peak is determined mainly by the stopping power, whereas its width can be attributed to the energy-loss straggling. Multiple elastic scattering processes contribute slightly only at the distal part of the Bragg peak. The charge state of the projectiles only changes when approaching the end of their trajectories, i.e. near the Bragg peak. We have also simulated the proton-beam energy distribution at several depths in the liquid water target, and found that it is determined mainly by the fluctuation in the energy loss of the projectile, evaluated through the energy-loss straggling. We conclude that a proper description of the target excitation spectrum as well

as the inclusion of the energy-loss straggling is essential in the calculation of the proton beam depth–dose distribution.

(Some figures in this article are in colour only in the electronic version)

1. Introduction

The study of the irradiation of biological materials with energetic protons (and heavier charged particles) has nowadays become of great interest due to its applications in ion-beam radiotherapy and space radiation protection (Goitein *et al* 2002, Brahme 2004, Podgoršak 2006, Nikjoo *et al* 2008a, Andreo 2009, Schardt *et al* 2010, Paganetti and Kooy 2010, Belkić 2010).

In order to predict the damage produced by energetic ions in a biological tissue it is necessary to understand the physical processes involved in the interaction of these projectiles with the biological target. The use of energetic protons (and heavier atomic projectiles, like carbon) in oncological treatments has important advantages if compared with conventional photon or electron beam therapy (Kiefer 2008, Blakely and Chang 2009). This is because photon or electron projectiles, at clinically relevant beam energies, deposit a high fraction of their energy near the surface of the biological tissue, causing undesirable damage in healthy tissues when treating deep-seated tumours. In order to minimize this damage, several photon and electron beams irradiating from different directions usually are needed (i.e. intensity modulated radiation therapy, IMRT). On the other side, high-energy protons have a well-defined penetration range, do not suffer significant angular scattering, and lose most of their energy in a well-localized region near the end of their trajectories. This pattern of energy deposition (known as the Bragg curve) results in a more favourable depth–dose profile for radiotherapy purposes, especially due to the distinct narrow peak (named the Bragg peak) at the end of the projectile path, which defines a localized region of the target where the energy delivered and the relative biological effectiveness are enhanced (Paganetti *et al* 2002). The position of the Bragg peak in the treated target can be precisely adjusted by varying the energy of the protons and therefore affecting malignant tumours while minimizing damage to healthy cells. In summary, the depth–dose curves from protons are much more suitable for tumour therapy than those from photon or electron beams (Kraft 2000, Smith 2006). Several general-purpose Monte Carlo simulation codes have been developed in the last years, like GEANT (Agostinelli *et al* 2003, Allison 2006), PENELOPE (Salvat *et al* 2003), PARTRAC (Friedland *et al* 2003), SHIELD-HIT (Gudowska *et al* 2004) or FLUKA (Sommerer *et al* 2006), which combine reliability and speed and provide essential data for medical physics and radiation protection; for a review see Nikjoo *et al* (2006). Recent efforts include the clinical implementation of Monte Carlo simulation codes for the support of treatment planning in proton beam radiotherapy (Fippel and Soukup 2004, Stankovskiy *et al* 2009, Paganetti and Kooy 2010) as well as the development of detailed track structure codes for full-slowing-down simulation of proton and secondary electron tracks in water (Champion *et al* 2005, Plante and Cucinotta 2008, Gonzalez-Muñoz *et al* 2008, Friedland *et al* 2011, Liamsuwan *et al* 2011).

The aim of this work is to analyse the main physical phenomena that affect and determine the energy deposited by a proton beam as a function of depth in soft tissue, approximated here by unit-density (1 g cm^{-3}) liquid water. We are particularly interested in studying the interactions that take place near the Bragg peak and in determining the energy deposited in the target around this depth, knowledge of which is essential in radiotherapy. For this

reason, we will deal with relatively low projectile energies around a few MeV instead of the higher beam energies commonly used in proton radiotherapy (∼70–250 MeV). Liquid water is chosen as the target because all living organisms are mainly composed of water (being also the source of highly reactive free radicals); therefore, therapeutic proton beams must travel through this stopping medium although the energy they deliver to subcellular structures (most notably to the DNA) is also important from a biophysical perspective (Nikjoo *et al* 2001, Paganetti 2005, Obolensky *et al* 2008, Solov'yov *et al* 2009, Lindborg and Nikjoo 2011). To that end, an important advantage of the present methodology is that it can be effectively applied for modelling the interactions (and energy deposition) of a proton beam with other condensed-phase biological targets (Abril *et al* 2011, de Vera *et al* 2011).

It should be mentioned that our study does not attempt a detailed description of electron exchange taking place close to the Bragg peak, where more sophisticated methodologies, like the continuum distorted wave approximation, are providing promising new results (Olivera *et al* 1996, Boudrioua *et al* 2007, Belkić *et al* 2008).

The main tool we use for this study is a simulation code named SEICS (Simulation of Energetic Ions and Clusters through Solids), which is based on a combination of molecular dynamics and Monte Carlo techniques to describe the projectile motion through the target (Heredia-Avalos *et al* 2007a). The SEICS code, whose features are described in the appendix, includes in a detailed manner both the interaction of the projectile with the target electrons (i.e. the stopping force, which is mainly responsible for the energy lost by the projectile), as well as the interaction with the target nuclei (i.e. the elastic scattering, which is mainly responsible for the beam angular spread). As the stopping force depends on the charge state of the projectile, we have also considered electron-capture and -loss by the projectile when it moves through the target. Taking into account all these processes, the SEICS code dynamically follows the motion of each projectile, providing its position, velocity and charge state at any time. With these data the code can evaluate very useful magnitudes for radiotherapy, namely, the spatial distribution of energy deposition, the energy distribution and the angular spread of the beam at a given depth, the penetration range, the average charge of the projectile as a function of the depth, etc.

In section 2, we discuss the calculation of the main stopping magnitudes (stopping power and energy-loss straggling), whose values determine the slowing down of protons in liquid water, and are the essential inputs into the SEICS code. A comparison with recent stopping power measurements of protons in liquid water is also shown. The results provided by the SEICS code for the depth–dose distributions and the energy distribution of protons in liquid water, together with a discussion of the influence of each interaction considered in the simulation, are discussed in section 3. Finally, we present the conclusions in section 4. The appendix contains a full description of the SEICS simulation code.

2. Inelastic energy-loss magnitudes of swift projectiles

When a swift atomic ion moves through a target (liquid water, in our case), it loses energy mainly due to inelastic collisions with the target electrons. Moreover, the projectile can change its charge state due to electronic capture and loss processes with the target electrons until reaching a dynamical equilibrium. The most important magnitudes that describe the electronic slowing down of the projectile are the stopping power (or stopping force) and the energy-loss straggling, both depending on the energy and charge state of the projectile, as well as on the target nature (Nastasi *et al* 1996, Sigmund 2006).

We apply the dielectric formalism to calculate the electronic stopping magnitudes, which is based on the plane-wave (first) Born approximation and consistently accounts for the

condensed-phase properties of liquid water (Lindhard 1954, Ritchie 1957). In this framework, a projectile with charge-state q, atomic number z and mass m moving with a kinetic energy E through a target characterized by its dielectric function, $\varepsilon(k,\omega)$, experiences a stochastic slowing down where the average value of the stopping power S_q is given by

$$S_q(E) = \frac{me^2}{\pi\, E}\int_0^\infty \frac{\mathrm{d}k}{k}\rho_q^2(k)\int_0^{k\sqrt{2E/m}} \mathrm{d}\omega\,\omega\,\mathrm{Im}\left[\frac{-1}{\varepsilon\,(k,\omega)}\right]. \tag{1}$$

The energy-loss straggling Ω_q^2, which is related to the width of the energy-loss distribution, can be calculated as

$$\Omega_q^2(E) = \frac{m\hbar e^2}{\pi\, E}\int_0^\infty \frac{\mathrm{d}k}{k}\rho_q^2(k)\int_0^{k\sqrt{2E/m}} \mathrm{d}\omega\,\omega^2\,\mathrm{Im}\left[\frac{-1}{\varepsilon\,(k,\omega)}\right]. \tag{2}$$

Here e is the elemental charge, and $\rho_q(k)$ is the Fourier transform of the projectile charge density for the charge-state q, which is calculated according to the modified Brandt–Kitagawa model (Brandt and Kitagawa 1982, Brandt 1982). In the above expressions, the only magnitude that depends on the target is the energy-loss function (ELF), $\mathrm{Im}[-1/\varepsilon(k,\omega)]$, which accounts for the probability that the projectile loses energy producing an electronic excitation with momentum transfer $\hbar k$ and energy transfer $\hbar\omega$ to the target.

On the other hand, when equilibrium of the projectile charge state is reached, the stopping power, S, and the energy-loss straggling, Ω^2, can be expressed as a weighted sum over these magnitudes for the different charge-states q of the projectile, namely

$$S(E) = \sum_{q=0}^{z}\phi_q(E)S_q(E), \qquad \Omega^2(E) = \sum_{q=0}^{z}\phi_q(E)\Omega_q^2(E), \tag{3}$$

with $\phi_q(E)$ being the probability of finding the projectile with a charge-state q, which varies with the energy and nature of the projectile and with the target. For a proton interacting with water, $\phi_q(E)$ is determined from a parameterization to experimental data given by Schiwietz and Grande (2001).

The stopping power and the energy-loss straggling of liquid water for protons are evaluated analytically using the Mermin energy loss function-generalized oscillators strengths (MELF-GOS) method (Abril *et al* 1998, Heredia-Avalos *et al* 2005) to describe the ELF of the target. In this model the inner-electron excitations from the oxygen K-shell are described through atomic GOS (generalized oscillator strengths), whereas the contribution of the remaining outer electrons are described by fitting the experimental ELF in the optical limit ($k = 0$) (Hayashi *et al* 2000) by a linear combination of Mermin-type ELF (Mermin 1970). The construction of ELF (or the dielectric response function) from experimental optical data along with methods to extend them to arbitrary momentum transfer ($k \neq 0$) has been successfully applied for calculating the inelastic interaction of energetic ions with various condensed-phase biomaterials (Dingfelder *et al* 2000, 2008, Emfietzoglou *et al* 2006, 2009, Tan *et al* 2010a, 2010b, Abril *et al* 2010, Scifoni *et al* 2010a, 2010b). The advantages of the MELF-GOS methodology consist of a realistic description of the experimental energy-loss spectrum, the inclusion of the finite lifetime of electronic excitations and an analytical extension of the ELF to finite momentum transfers without *ad hoc* suppositions for the k-dependence of the dielectric function (Emfietzoglou *et al* 2005, Garcia-Molina *et al* 2011). The ELF for liquid water obtained within the MELF-GOS model (Emfietzoglou *et al* 2008, Garcia-Molina *et al* 2009) shows very good agreement with the experimental ELF data for liquid water at all values of momentum transfer k (Watanabe *et al* 1997).

In figure 1(a) we show the stopping power of liquid water for protons as a function of their incident energy. In addition to its importance in SEICS, the stopping power represents the

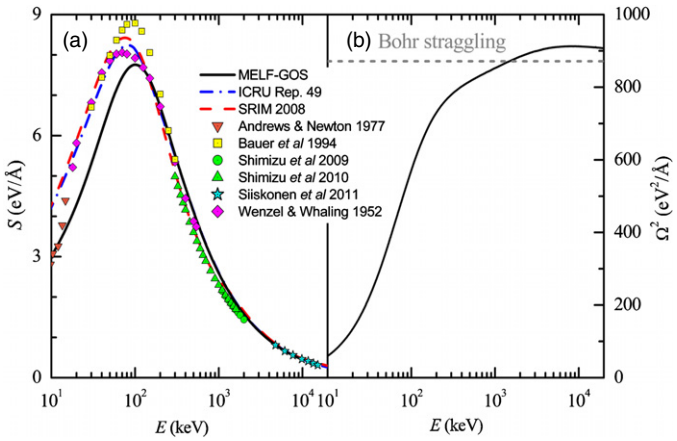

Figure 1. (a) Stopping power of liquid water for protons as a function of their incident energy. Symbols are the experimental data for liquid water (Shimizu *et al* 2009, 2010, Siiskonen *et al* 2011) and for ice (Wenzel and Whaling 1952, Andrews and Newton 1977, Bauer *et al* 1993). The curves represent calculations obtained using the MELF-GOS model (Garcia-Molina *et al* 2009) (solid line), the data compiled in the ICRU Report 49 (ICRU 1993) (dashed-dotted line) and the semiempirical SRIM code (Ziegler *et al* 2008) (dashed line). (b) Energy-loss straggling of liquid water for protons as a function of their incident energy obtained with the MELF-GOS model. The horizontal dashed line represents the Bohr energy-loss straggling.

most fundamental magnitude in the clinical dosimetry protocols for proton beam radiotherapy. Thus, any uncertainty in the stopping power directly translates to uncertainties in patient dosimetry. The solid line represents our calculations, equations (1) and (3), using the MELF-GOS model (Garcia-Molina *et al* 2009), whereas symbols are the experimental data for liquid water targets (Shimizu *et al* 2009, 2010, Siiskonen *et al* 2011) and ice targets (Wenzel and Whaling 1952, Andrews and Newton 1977, Bauer *et al* 1993). For comparison purposes, we also depict as a dashed line the semiempirical results provided by the SRIM code (Ziegler *et al* 2008) and as a dashed–dotted line the stopping power compiled in the ICRU Report 49 (ICRU 1993). A more complete compilation of different experimental and theoretical data for liquid water can be found elsewhere (Paul 2010). We find excellent agreement of our MELF-GOS model calculations with the newest experimental data in liquid water at high proton energies (Siiskonen *et al* 2011), which means that the mean excitation energy I of liquid water calculated using the MELF-GOS model, $I = 79.4$ eV (Garcia-Molina *et al* 2009), is in good agreement with the trends of the recent results. The spread in the available I-value of liquid water (see, for example, the compilation in Paul *et al* (2007a, 2007b)) has been recognized as particularly disturbing due to its effect on the Bethe stopping power formula and the ion range (Paul *et al* 2007a, 2007b, Andreo 2009). The calculated stopping power by the MELF-GOS model at lower energies differs from the available experimental data of protons in ice, which could be mainly attributed to differences between the energy-loss spectrum of liquid water and ice (Garcia-Molina *et al* 2011). Both SRIM and ICRU data provide good agreement with the experimental data for ice, because they use a parameterization to these available experimental data.

We depict in figure 1(b) the energy-loss straggling for protons moving through liquid water calculated by the MELF-GOS method in a wide range of projectile incident energies (see the appendix for more details). Unfortunately, in this case there are no experimental data to compare with. We show by a dashed line the Bohr energy-loss straggling, valid at high energies,

which is given by $\Omega^2_{\mathrm{Bohr}} = 4\pi z^2 Z e^2 N$, where $Z = 10$ and $N = 3.34 \times 10^{22}$ molecules cm^{-3} are the atomic number and the molecular density, respectively, of the liquid water target.

3. Simulation of depth–dose distributions: results and discussion

The SEICS code has been applied to calculate the spatial distribution of the energy delivered by a proton beam travelling in liquid water as a function of depth. Besides, the energy distribution of the initial monoenergetic proton beam is obtained at several depths.

Although a detailed explanation of the simulation code is provided in the appendix, in what follows we comment on its main features. The SEICS code simulates the motion of each incident proton through the target, taking into account in a detailed manner the interactions it suffers. The classical trajectory of the projectile is calculated numerically by solving its equation of motion, by a finite differences algorithm, until it reaches a threshold energy E_{th}; we use $E_{\mathrm{th}} \sim 250$ eV, although reducing this value is of no consequence in the final depth–dose distributions. Proceeding in this manner we know the coordinates and the velocity of the projectile at each time and, subsequently, the deposited energy by the projectile into the irradiated target, as well as the energy distribution of the initially collimated beam, can be found as a function of the depth. The code includes the self-retarding stopping force (experienced by the projectile due to electronic interactions), equation (1), with statistical fluctuations around the mean energy-loss value provided by the energy-loss straggling, equation (2). The multiple elastic scattering of the projectile with the target nuclei is also accounted for through a Monte Carlo algorithm. This latter process is mainly responsible for the angular deflection of the projectile and also contributes significantly to its energy loss at low projectile energy, i.e. around the distal part of the Bragg peak. Besides, electronic capture and loss processes are considered along the projectile path, dynamically varying its charge state as it moves through the target, which leads to corresponding changes of the stopping power and the energy-loss straggling.

In all the simulations carried out in this work the stopping power, S_q, and the energy-loss straggling, Ω^2_q, for each charge-state q, which are input quantities required in the SEICS code, have been calculated by equations (1) and (2) and using the MELF-GOS method to describe realistically the ELF of liquid water.

The simulated depth–dose distribution of a 3 MeV proton-beam in liquid water is depicted in figure 2. In order to visualize how the elastic scattering processes and the energy-loss straggling affect the spatial distribution of the energy deposition, the solid line in figure 2 shows the depth–dose distribution when all the interactions are included in the simulation, whereas dashed and dotted lines are the results obtained when removing the elastic scattering processes or the energy-loss straggling, respectively. We find that the plateau of the Bragg curve is mainly determined by the electronic stopping force, with the elastic scattering and the energy-loss straggling having negligible effects before the projectile reaches the region around the Bragg peak. The removal of elastic scattering in the simulation moves the Bragg peak distal-edge a bit deeper, since it is the elastic scattering which is mainly responsible for the projectile slowing down at low energies, i.e. at the end of its trajectory. Removing the fluctuations of the projectile energy loss along its full path (accounted for by the energy-loss straggling) produces a deeper (around 2%) and a much sharper peak with a steep fall-off, as can be observed in figure 2. Therefore, the results depicted in figure 2 clearly indicate that elastic scattering and mainly energy-loss straggling are crucial to determine the position and shape of the Bragg peak, although their contribution to the plateau of the Bragg curve is not critical.

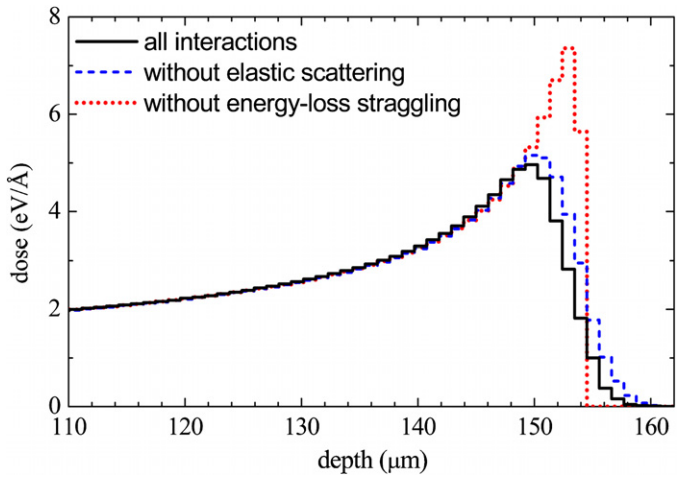

Figure 2. Depth–dose distribution corresponding to a 3 MeV proton-beam in liquid water. The solid line is the calculation when all the contributions are included in the simulation, whereas the dashed and dotted curves are the results obtained when the elastic scattering processes and the energy-loss straggling are removed, respectively, from the simulations.

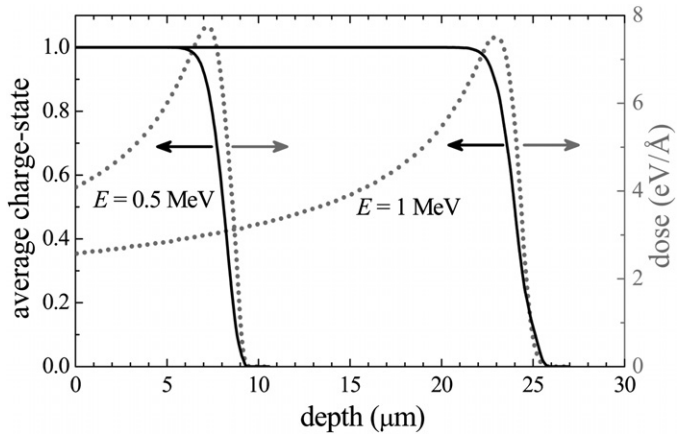

Figure 3. (Left axis): average charge state of 0.5 and 1 MeV proton beams as a function of depth in a liquid water target. For comparison purposes we represent, by a dotted line, the depth–dose distribution (right axis).

We show in figure 3 the average charge state for 0.5 and 1 MeV proton-beams as a function of the depth in liquid water; for comparison purposes we also depict the corresponding depth–dose distributions as dotted curves. Although electron capture and loss processes between the projectile and the target are taking place during all the projectile travel, a dynamical equilibrium is quickly reached, and the projectile moves as a bare proton during most of its trajectory (for energies larger than 250 keV). Only near the Bragg peak and, in particular, at the end of the trajectory does the average charge of the projectile decrease. This explains the similar shape obtained for the average charge state of 0.5 and 1 MeV proton beams. It is worth mentioning that this behaviour could be also observed for higher energy protons: they travel as protons until the end of their trajectories, when the fraction of neutral hydrogen

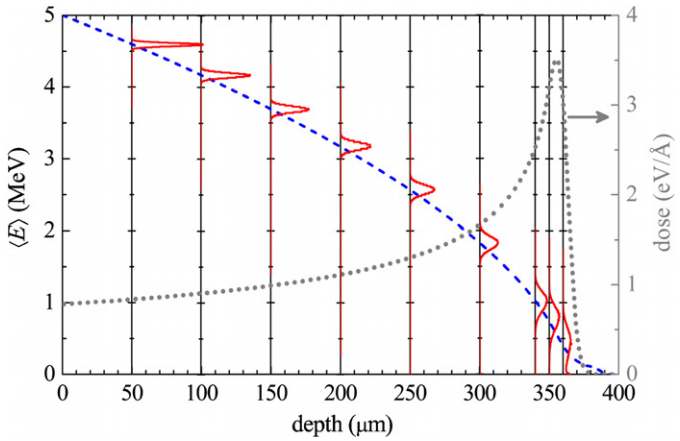

Figure 4. (Left axis): average energy (dashed line) for a 5 MeV proton beam as a function of the depth in liquid water. The proton energy distributions are depicted by solid lines at several depths. For comparison the depth–dose distribution (right axis) is shown by a dotted line.

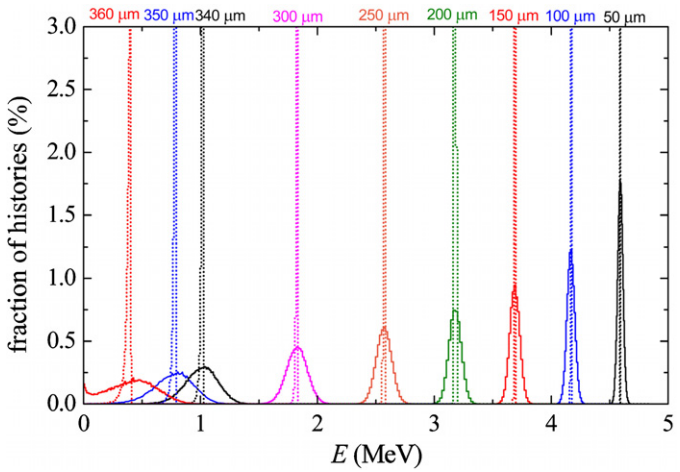

Figure 5. Energy distributions of 5 MeV protons in liquid water at several target depths. The solid curves correspond to the simulations when all the interactions are included, whereas dotted curves represent the results without energy-loss straggling.

atoms becomes significant and, therefore, the projectile average charge decreases. It is worth mentioning that neither multiple scattering nor energy-loss straggling influences the results of the simulations for the average charge state.

As the energy loss magnitudes depend on the projectile charge state, a detailed evaluation of the energy delivered by the projectile around the Bragg peak at a nano and/or micrometric scale must take into account both the electron charge-exchange processes and the fluctuations in the projectile energy loss at each inelastic collision.

We show in figure 4 the average energy (dashed line) and the energy distribution (solid lines) corresponding to a 5 MeV proton beam as a function of the depth in liquid water. For comparison the depth–dose distribution is represented by a dotted line at the right axis.

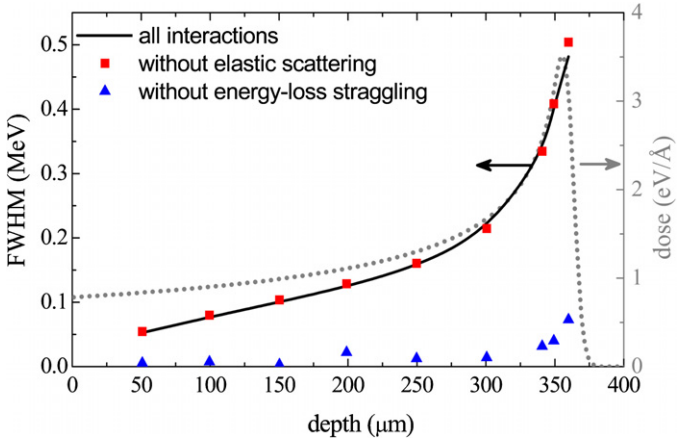

Figure 6. (Left axis): FWHM of the energy distributions corresponding to a 5 MeV proton beam as a function of the depth in liquid water. The solid curve represents the results obtained when considering all interactions in the simulations, whereas squares and triangles are the results obtained when elastic scattering and energy-loss straggling are removed, respectively, from the simulation. For comparison the depth–dose distribution is shown by a dotted line (right axis).

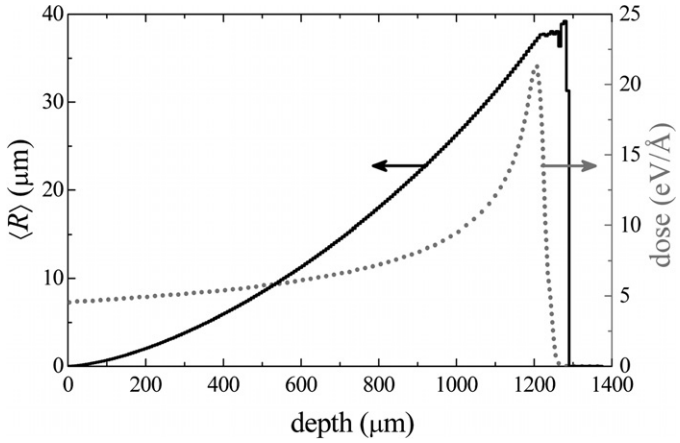

Figure 7. (Left axis): mean radius of a 10 MeV proton beam as a function of the depth in liquid water. (Right axis): depth–dose distribution is shown by a dotted line.

As expected, the average energy of protons decreases with depth, mainly due to inelastic collisions with target electrons (i.e. electronic excitations and ionizations). This figure also shows that the Bragg peak occurs when the energy of the proton beam is lower than 1 MeV, which corresponds to the growing part of the stopping power curve when the projectile energies diminishes (see figure 1).

The energy distribution of the initially monoenergetic proton beam at several depths in liquid water becomes broader as the depth inside the target increases, as can be seen in figure 4. Since the proton energy distribution determines the generation of secondary electrons in the target, which are mainly responsible for the DNA damage (Nikjoo *et al* 1998, 2008b, Champion *et al* 1998, Uehara *et al* 2001, Sanche 2005), it is worth considering how the

different interactions in our simulation affect the proton energy distribution. Note that at the Bragg peak, the projectile energy distributions are not symmetric since at these depths the projectiles start to stop, increasing the contribution to histogram bins corresponding to lower energies.

In figure 5, we depict the simulated energy distribution for a 5 MeV proton-beam at different depths inside the liquid water target, with emphasis around the Bragg peak. Solid lines represent the results obtained when all interactions are included in the simulation, whereas the dotted lines represent the results obtained removing energy-loss straggling from the simulation code; the results obtained when multiple scattering is not taken into account are almost indistinguishable from the full simulation curves. The results show that elastic scattering processes do not change the projectile energy distribution to any significant extent, whereas energy-loss straggling (accounting for the fluctuations in the projectile energy loss) is mainly responsible for the broadening of the proton energy distribution. Note that the increase in the fraction of histories observed at the low-energy side of the proton energy distribution at 360 μm (corresponding to the distal part of the Bragg peak) can be attributed to the significant fraction of 'almost' stopped projectiles at such depth.

The full width at half maximum (FWHM) of the proton energy distribution as a function of the liquid water depth is shown in figure 6, as well as the depth–dose distributions (dotted line) for the same system as in figure 5. The FWHM is depicted by a solid line when all the interactions are considered in the simulation, whereas squares and triangles are the results obtained when the simulation does not include multiple scattering and energy-loss straggling, respectively. No significant differences in the FWHM are observed whether or not elastic scattering is included in the simulations; however, sizeable differences appear when considering or not energy-loss straggling.

In order to analyse how the radial (i.e. lateral) broadening of an initial pencil beam evolves inside the target, we have depicted in figure 7 the mean radius of a 10 MeV proton beam as a function of the depth in liquid water. Due to multiple elastic collisions the mean radius of the beam follows an increasing trend as a function of depth travelled in the medium, which is nearly a parabolic function. The mean radius of the proton beam becomes approximately constant near the Bragg peak, with a sharp reduction at the distal region, which can be attributed to the fact that only (few) projectiles travelling in almost a straight path reach these deep regions. As most of the projectiles deviate from their initial direction, they are stopped at lower depths.

4. Conclusions

We have obtained the spatial distribution of the energy deposition by proton beams in liquid water using the simulation code SEICS, which includes the stopping force due to the target electronic excitations induced by the projectile and their fluctuations in the energy loss, the multiple elastic scattering with the target nuclei and the changes in projectile charge-state due to electronic capture and loss processes.

The inelastic energy loss magnitudes for proton beams in liquid water, such as the stopping power and the energy-loss straggling, which are basic inputs for any simulation code, are calculated using a solid-state perspective of the beam–target interaction within the dielectric formalism together with the MELF-GOS methodology to properly describe the ELF of liquid water. Our calculated stopping power agrees very well with recent experimental data (Siiskonen *et al* 2011), providing a validation of the mean ionization energy of liquid water ($I = 79.4$ eV) given by our model.

We have found that the position of the Bragg peak is mainly determined by the stopping power of the projectile, whereas its shape strongly depends on the energy-loss straggling.

The multiple scattering processes only modify the distal part of the Bragg peak, at the end of the projectile trajectories. Also, the average charge state of the projectile has been obtained, concluding that the projectile travels most of the time as a bare charge, but around the Bragg peak the average charge decreases, due to a significant presence of neutral hydrogen.

The energy distribution of the proton-beam at several depths is also calculated by the simulation code SEICS. We find that elastic collisions are practically irrelevant; however, the proton energy profile strongly depends on the statistical fluctuations of the projectile slowing down, which is accounted for through the energy-loss straggling.

The radial broadening of the proton beam, mainly due to elastic collisions, increases with the depth, according to a parabolic dependence.

From these simulations we conclude that for a realistic evaluation of the Bragg peak at the microdosimetric level a detailed account of the electronic response and condensed-phase excitation properties of the target is necessary, as for example provided by our simulation code SEICS. Further improvements with the addition of secondary electron generation and transport, as well as an extension to higher proton energies (with the inclusion of nuclear interactions) are underway.

Acknowledgments

Support from the Spanish Ministerio de Ciencia e Innovación (Project FIS2010-17225) is recognized. IK and DE acknowledge support from the European Union FP7 ANTICARB (HEALTH-F2-2008-201587). This work is part of the COST Action MP 1002, Nanoscale Insights into Ion Beam Cancer Therapy.

Appendix. SEICS code

The SEICS code uses molecular dynamics and Monte Carlo techniques to follow the motion of a charged projectile through a target (Heredia-Avalos *et al* 2007a). This procedure provides the position and velocity at any time along the trajectory of each projectile through the target. Therefore, it is straightforward to obtain the beam energy and spreading as a function of the depth, or the spatial distribution of deposited energy, among other quantities. Although the SEICS code can be applied to any projectile–target combination, including molecular projectiles and compound targets, in what follows we will particularize the discussion for the case of monatomic ions moving through a liquid water target.

Electronic stopping force

Leaving aside for a moment the elastic collisions between the projectile and the atomic nucleus (to be discussed in the next section), the force that acts on the projectile is given by the electronic stopping force, which depends on its charge state and velocity, and arises from the inelastic collisions between the projectile and the target electrons. Here we use a model based on the dielectric formalism to calculate this electronic stopping force (Lindhard 1954, Ritchie 1957). Once the stopping force is provided, the slowing down of the projectile is accounted for by numerically solving its equations of motion at discrete time intervals Δt. Due to the stochastic nature of the interaction between the target electrons and the projectile (with charge-state q), there are fluctuations in the force felt by the latter; therefore, we characterize the stopping force by an average value, the well-known stopping power, S_q, and the energy-loss straggling, Ω_q^2, given respectively by equations (1) and (2).

In the stopping magnitudes, the ELF over the whole k–ω plane is described by the MELF-GOS method, where a split between the outer electron excitations and the inner shell electrons is made (Abril *et al* 1998, Heredia-Avalos *et al* 2005):

$$\mathrm{Im}\left[\frac{-1}{\varepsilon(k,\omega)}\right] = \mathrm{Im}\left[\frac{-1}{\varepsilon(k,\omega)}\right]_{\mathrm{outer}} + \mathrm{Im}\left[\frac{-1}{\varepsilon(k,\omega)}\right]_{\mathrm{inner}}. \tag{A.1}$$

The most external electrons are modelled by a sum of Mermin-type ELF fitted to available experimental ELF at the optical limit ($k = 0$), namely

$$\mathrm{Im}\left[\frac{-1}{\varepsilon(k,\omega)}\right]_{\mathrm{outer}} = \sum_i A_i \mathrm{Im}\left[\frac{-1}{\varepsilon_{\mathrm{M}}(\omega_i,\gamma_i;k,\omega)}\right]\Theta(\omega-\omega_{\mathrm{th},i}), \tag{A.2}$$

where ω_i, γ_i and A_i are the fitting parameters related to the position, width and relative intensity of the peaks observed in the experimental optical ELF spectrum; $\omega_{\mathrm{th},i}$ is a threshold energy (7 eV for liquid water). ε_{M} is the Mermin dielectric function (Mermin 1970), which includes the damping of the electronic excitations through phonon-assisted electronic transitions, and is given in terms of the Lindhard dielectric function ε_{L} (Lindhard 1954) by the following expression:

$$\varepsilon_{\mathrm{M}}(k,\omega) = 1 + \frac{(1+\mathrm{i}\gamma\hbar/\omega)\,[\varepsilon_{\mathrm{L}}(k,\omega+\mathrm{i}\gamma)-1]}{1+(\mathrm{i}\gamma\hbar/\omega)\,[\varepsilon_{\mathrm{L}}(k,\omega+\mathrm{i}\gamma)-1]/[\varepsilon_{\mathrm{L}}(k,0)-1]}. \tag{A.3}$$

The inner shell electron excitations preserve their atomic character. Therefore, they are described by the GOS in the hydrogenic approach

$$\mathrm{Im}\left[\frac{-1}{\varepsilon(k,\omega)}\right]_{\mathrm{inner}} = \frac{2\pi^2 N}{\omega}\sum_j \alpha_j \sum_{nl}\frac{\mathrm{d}f_{nl}^j(k,\omega)}{\mathrm{d}\omega}\Theta(\omega-\omega_{\mathrm{ioniz},nl}), \tag{A.4}$$

where N is the molecular density of the target (for water $N = 3.34\times10^{22}$ molecules cm^{-3}), $\mathrm{d}f_{nl}^j(k,\omega)/\mathrm{d}\omega$ is the hydrogenic GOS corresponding to the (n,l)-subshell of the jth element, $\omega_{\mathrm{ioniz},nl}$ is the ionization energy of the (n,l)-subshell and α_j indicates the stoichiometry of the jth element in the compound target. For liquid water, the K-shell electrons of oxygen are treated as inner electrons with a binding energy of 540 eV.

Also, the MELF-GOS methodology imposes that the fitted ELF must verify physical constraints, such as the f-sum rule and the Kramers–Kronig (or perfect) sum rule, which guarantee correct behaviour at high and low energy transfer, respectively. Besides, if the sum rules are satisfied at $k = 0$ they will be verified at every momentum transfer.

In the simulation we take the modulus of the electronic stopping force felt by the projectile (with charge state q) from a Gaussian distribution with mean value S_q, and standard deviation

$$\sigma = \sqrt{\Omega_q^2/\Delta s}, \tag{A.5}$$

with $\Delta s = v\Delta t$ being the distance travelled by the projectile (with velocity v) in a time step Δt used to discretize the equations of motion. Therefore, according to the Box–Muller procedure to generate a Gaussian distribution (Box and Muller 1958), the electronic stopping force on the projectile enters the simulation code as

$$\vec{F} = -[S_q + (\Omega_q/\sqrt{\Delta s})\,\sqrt{-2\ln\xi_1}\cos(2\pi\xi_2)]\,\hat{v}, \tag{A.6}$$

where $\hat{v}$ is the unit vector of the instantaneous projectile velocity $\vec{v}$. The symbols ξ_i (with $i = 1, 2, \ldots$) refer to random numbers uniformly distributed between 0 and 1 (Press *et al* 1997), with the value of the subscript i denoting each time a random number ξ_i is used in the simulation.

Elastic scattering

Elastic scattering due to collisions between the projectile and the target atomic cores (Möller *et al* 1975, Zajfman *et al* 1990) are simulated in SEICS in a manner that provides the projectile scattering angle and the corresponding elastic energy loss at each collision. In this treatment, the path length L of the projectile between two successive collisions with the target atoms is given by

$$L = -\frac{\ln \xi_3}{\sum_i \mu_i}, \tag{A.7}$$

where μ_i is the projectile inverse mean free path for having an elastic interaction with the i-atom of the target compound. Therefore $\sum_i \mu_i$ is the total macroscopic cross section for having an elastic collision with a target nucleus.

Assuming that each target atom is an effective scattering centre with a spherical volume with radius $r_0 = 1/(2N^{1/3})$, where N is the target molecular density, then we can write

$$\mu_i = N_i \pi r_0^2 = \frac{\pi}{4N^{2/3}} N_i, \tag{A.8}$$

where N_i is the atomic density of the i-atom type in the target compound. For a liquid water target we have $N_{H_2O} = N_O = N_H/2$.

In order to determine the type of target atom that undergoes the collision with the projectile, we suppose that the collision probability P_i with the i-atom type is proportional to the fractional contribution made by each atom to the total cross section (Turner *et al* 1985):

$$P_i = \frac{\mu_i}{\sum_j \mu_j}. \tag{A.9}$$

Therefore, the projectile collides with the i-atom type of the target when the following condition is satisfied:

$$\sum_{j=1}^{i-1} P_j \leqslant \xi_4 < \sum_{j=1}^{i} P_j. \tag{A.10}$$

On the other hand, the polar scattering angle ϑ relative to the projectile direction of motion is given as a function of the parameter η through

$$\cos\vartheta = \left(1 - \frac{2M_i\eta^2}{(m+M_i)\mathcal{E}_i^2}\right)\left[1 - \frac{4mM_i\eta^2}{(m+M_i)^2\mathcal{E}_i^2}\right]^{-1/2}, \tag{A.11}$$

where m is the projectile atomic mass and M_i is the atomic mass of the i-atom type of the target compound; $\mathcal{E}_i$ is the corresponding reduced energy defined by

$$\mathcal{E}_i = \frac{a_{U,i} M_i}{z\, Z_i (m + M_i)} E, \tag{A.12}$$

with E being the projectile instantaneous kinetic energy, z and Z_i being the projectile and i-atom type target atomic numbers, and $a_{U,i}$ being the corresponding universal screening length (Ziegler *et al* 2008):

$$a_{U,i} = \frac{0.8853}{z^{0.23} + Z_i^{0.23}}. \tag{A.13}$$

The value of the parameter η in equation (A.11) is calculated using the scattering cross section in reduced units:

$$J(\eta) = J(\mathcal{E}_i) + \frac{1 - \xi_5}{4N^{2/3}\, a_{U,i}^2}. \tag{A.14}$$

$J(\eta)$ can be evaluated using

$$J(\eta) = J(\eta_0) + \int_{\eta_0}^{\eta} \mathrm{d}\eta' \frac{f(\eta')}{\eta'^2}, \tag{A.15}$$

$f(\eta)$ being a function given by Meyer (1971) and we assume $\eta_0 = 10^{-4}$ as a fixed lower integration limit. Note that equation (A.14) is independent of η_0, because both $J(\eta)$ and $J(\mathcal{E}_i)$ depend on η_0 through equation (A.15). We have evaluated the function $J(\eta)$ according to equation (A.15) and tabulated its values in order to obtain the value $J(\mathcal{E}_i)$ required in equation (A.14) to calculate $J(\eta)$; then, the value of η, used in equation (A.15) to determine the scattering angle θ, is obtained by interpolation of the tabulated function $J(\eta)$.

The azimuthal scattering angle ψ relative to the projectile direction of motion is simply

$$\varphi = 2\pi\xi_6. \tag{A.16}$$

Finally, the energy loss in the scattering process is obtained through

$$T = \frac{4mzZ_i}{a_{\mathrm{U},i}\mathcal{E}_i(m + M_i)}\eta^2, \tag{A.17}$$

so the modulus of the projectile velocity after the elastic nuclear collision takes place will be

$$v' = \sqrt{v^2 - \frac{2T}{m}}. \tag{A.18}$$

The geometry of the scattering process is depicted schematically in figure A1. We define the projectile direction of motion after the n-collision by the polar angle Θ_{n-1} and the azimuthal angle Ψ_{n-1} in the laboratory frame of reference. The path length L until the next elastic collision is determined by using equation (A.7); after an elapsed time L/v, the n-collision takes place and we determine the i type of target atom that is involved in the collision according to equation (A.10). Then, the scattering angles ϑ and φ, with respect to the direction of motion, are obtained using equations (A.11) and (A.16), respectively, and the new direction of the projectile after the n-collision is obtained through (Zajfman *et al* 1990)

$$\cos\Theta_n = -\sin\vartheta\cos\varphi\sin\Theta_{n-1} + \cos\vartheta\cos\Theta_{n-1} \tag{A.19}$$

$$\begin{aligned}\cos\Psi_n = \frac{1}{\sin\Theta_n}\,&(\sin\vartheta\cos\varphi\cos\Theta_{n-1}\cos\Psi_{n-1} \\ &- \sin\vartheta\sin\varphi\sin\Psi_{n-1} + \cos\vartheta\sin\Theta_{n-1}\cos\Psi_{n-1})\,.\end{aligned} \tag{A.20}$$

The modulus of the projectile velocity after the n-collision is obtained using equation (A.18). Once the velocity (modulus and direction) is obtained after the n-collision, the next collision takes place following the same steps that have been explained in the preceding paragraphs.

Electron capture and loss

We have also included in SEICS the capture and loss of electrons by the projectile (Heredia-Avalos *et al* 2007a). In the model we have used, the path length of the projectile between two successive electronic capture or loss events is given by

$$L_{\mathrm{C\&L}} = -\frac{\ln\xi_7}{\mu_{\mathrm{C}} + \mu_{\mathrm{L}}}, \tag{A.21}$$

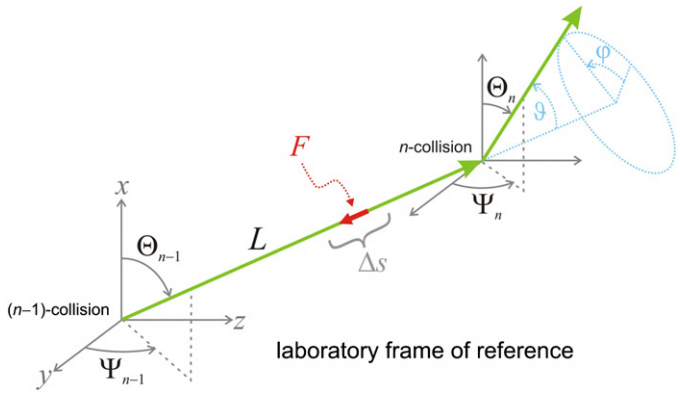

Figure A1. Schematic geometry of two successive elastic collisions, separated by a distance L, given by equation (A.7). The angles in the laboratory frame of reference that determine the projectile direction of motion before $(\Theta_{n-1}, \Psi_{n-1})$ and after (Θ_n, Ψ_n) the n-collision are related to the angles (ϑ, φ) with respect to the instantaneous velocity through equations (A.19) and (A.20). During the path L between two successive elastic collisions, the projectile (with charge state q) experiences a retarding force F that depends on its instantaneous velocity along each infinitesimal segment Δs, as given by equation (A.7); see text for more details.

where μ_C and μ_L are the inverse mean free paths for electron capture and electron loss, respectively, both depending on the charge-state q of the projectile. The inverse mean free path for electron loss μ_L can be evaluated through

$$\mu_L(q \to q+1) = N\sigma_L(q \to q+1), \tag{A.22}$$

where $q \to q+1$ denotes that the projectile changes its charge state from q to $q+1$.

In the model we have used, we assume that the electron-loss cross section σ_L is proportional to both the geometrical cross section σ of the projectile and its bound electrons,

$$\sigma_L(q \to q+1) = (z-q)\sigma, \tag{A.23}$$

where we estimate the geometrical cross section of the projectile using

$$\sigma = \pi\langle r\rangle^2 = 4\pi\Lambda^2, \tag{A.24}$$

with $\langle r\rangle = 2\Lambda$ being the average distance between the bound electrons and the atomic nucleus in the modified Brandt–Kitagawa model (Brandt and Kitagawa 1982, Brandt 1982).

If multiple-electron processes are neglected, the inverse mean free path for electron capture can be obtained from the equilibrium relation

$$\mu_C(q+1 \to q) = \frac{\phi(q)}{\phi(q+1)}\,\mu_L(q \to q+1), \tag{A.25}$$

where $\phi(q)$ and $\phi(q+1)$ are the equilibrium fractions of the q and $q+1$ charge states, respectively. These charge-state fractions $\phi(q)$ should be evaluated depending on the projectile atomic number. For hydrogen projectiles,

$$\phi(0) + \phi(+1) = 1, \tag{A.26}$$

$$\phi(+1) = \langle q\rangle, \tag{A.27}$$

where $\langle q\rangle$ is the average charge state. For helium projectiles, the conditions are

$$\phi(0) + \phi(+1) + \phi(+2) = 1, \tag{A.28}$$

$$\phi(+1) + 2\phi(+2) = \langle q\rangle, \tag{A.29}$$

$$\langle q\rangle^2\phi(0) + (1-\langle q\rangle)^2\phi(+1) + (2-\langle q\rangle)^2\phi(+2) = \sigma_q^2, \tag{A.30}$$

with σ_q being the standard deviation of the charge-states distribution. The charge-state fractions $\phi(q)$ for heavier projectiles can be calculated assuming a Gaussian distribution

$$f(q) = \frac{1}{\sqrt{2\pi\sigma_q^2}}\exp\left[-\frac{(q-\langle q\rangle)^2}{2\sigma_q^2}\right], \tag{A.31}$$

where $\phi(q)$ are then evaluated using

$$\phi(q) = \frac{f(q)}{\sum_{q=0}^{z} f(q)}, \tag{A.32}$$

in order to ensure that the charge fractions satisfy the normalization condition

$$\sum_{q=0}^{z}\phi(q) = 1. \tag{A.33}$$

In all these cases, both the average charge-state $\langle q\rangle$ and the standard deviation σ_q are obtained through a fit to experimental data (Schiwietz and Grande 2001).

The probabilities of electron loss P_{L} or electron capture P_{C} by a projectile with charge-state q are proportional to the corresponding inverse mean free paths

$$P_{\mathrm{L}}(q \to q+1) = \frac{\mu_{\mathrm{L}}(q \to q+1)}{\mu_{\mathrm{C}}(q \to q-1) + \mu_{\mathrm{L}}(q \to q+1)} \tag{A.34}$$

$$P_{\mathrm{C}}(q \to q-1) = 1 - P_{\mathrm{L}}(q \to q+1). \tag{A.35}$$

Therefore, in order to determine the new projectile charge-state q' we use the following condition:

$$q' = \begin{cases} q+1 & \text{for} \quad \xi_8 \leqslant P_{\mathrm{L}}(q \to q+1) \\ q-1 & \text{for} \quad \xi_8 > P_{\mathrm{L}}(q \to q+1). \end{cases} \tag{A.36}$$

In summary, according to this model we obtain the path length $L_{\mathrm{C\&L}}$ using equation (A.21); after an elapsed time $L_{\mathrm{C\&L}}/v$, either an electronic capture or loss event takes place determined according to equation (A.36).

References

Abril I, Denton C D, de Vera P, Kyriakou I, Emfietzoglou D and Garcia-Molina R 2010 Effect of the Bethe surface description on the electronic excitations induced by energetic proton beams in liquid water and DNA *Nucl. Instrum. Methods* B **268** 1763–7

Abril I, Garcia-Molina R, Denton C D, Kyriakou I and Emfietzoglou D 2011 Energy loss of hydrogen- and helium-ion beams in DNA: calculations based on a realistic energy-loss function of the target *Radiat. Res.* **175** 247–55

Abril I, Garcia-Molina R, Denton C D, Pérez-Pérez F J and Arista N R 1998 Dielectric description of wakes and stopping powers in solids *Phys. Rev.* A **58** 357–66

Agostinelli S *et al* 2003 Geant4—a simulation toolkit *Nucl. Instrum. Methods* A **506** 250–303

Allison J 2006 Geant4 developments and applications *IEEE Trans. Nucl. Sci.* **53** 270–8

Andreo P 2009 On the clinical spatial resolution achievable with protons and heavier charged particle radiotherapy beams *Phys. Med. Biol.* **54** N205–15

Andrews D A and Newton G 1977 The stopping power of heavy ice for low-energy (10–30 keV) deuterons *J. Phys. D: Appl. Phys.* **10** 845–50

Bauer P, Kaferbock W and Necas V 1993 Investigation of the electronic energy loss of hydrogen ions in H_2O: influence of the state of aggregation *Nucl. Instrum. Methods* B **93** 132–6

Belkić D 2010 Review of theories on ionization in fast ion–atom collisions with prospects for applications to hadron therapy *J. Math. Chem.* **47** 1366–419

Belkić D, Mančev I and Hanssen J 2008 Four-body methods for high-energy ion–atom collisions *Rev. Mod. Phys.* **80** 249–314

Blakely E A and Chang P Y 2009 Biology of charged particles *Cancer J.* **15** 271–84
Boudrioua O, Champion C, Dal Cappello C and Popov Y V 2007 *Ab initio* calculation of differential and total cross sections for the ionization of water vapor by protons *Phys. Rev.* A **75** 022720
Box G E P and Muller M E 1958 A note on the generation of random normal deviates *Ann. Math. Stat.* **29** 610–1
Brahme A 2004 Recent advances in light ion radiation therapy *Int. J. Radiat. Oncol. Biol. Phys.* **58** 603–16
Brandt W 1982 Effective charges of ions and the stopping power of dense media *Nucl. Instrum. Methods* **194** 13–9
Brandt W and Kitagawa M 1982 Effective stopping-power charges of swift ions in condensed matter *Phys. Rev.* B **25** 5631–7
Champion C, L'Hoir A, Politis M F, Chetioui A, Fayard B and Touati A 1998 Monte-Carlo simulation of ion track structure in water: ionization clusters and biological effectiveness *Nucl. Instrum. Methods* B **146** 533–40
Champion C, L'Hoir A, Politis M F, Fainstein P D, Rivarola R D and Chetioui A 2005 A Monte Carlo code for the simulation of heavy-ion tracks in water *Radiat. Res.* **163** 222–31
de Vera P, Abril I and Garcia-Molina R 2011 Inelastic scattering of electron and light ion beams in organic polymers *J. Appl. Phys.* **109** 094901
Dingfelder M, Inokuti M and Paretzke H G 2000 Inelastic-collision cross sections of liquid water for interactions of energetic protons *Radiat. Phys. Chem.* **59** 255–75
Dingfelder M, Ritchie R H, Turner J E, Friedland W, Paretzke H G and Hamm R N 2008 Comparisons of calculations with PARTRAC and NOREC: transport of electrons in liquid water *Radiat. Res.* **169** 584–94
Emfietzoglou D, Abril I, Garcia-Molina R, Petsalakis I D, Nikjoo H, Kyriakou I and Pathak A 2008 Semi-empirical dielectric descriptions of the Bethe surface of the valence bands of condensed water *Nucl. Instrum. Methods* B **266** 1154–61
Emfietzoglou D, Cucinotta F A and Nikjoo H 2005 A complete dielectric response model for liquid water: a solution of the Bethe ridge problem *Radiat. Res* **164** 202–11
Emfietzoglou D, Garcia-Molina R, Kyriakou I, Abril I and Nikjoo H 2009 A dielectric response study of the electronic stopping power of liquid water for energetic protons and a new *I*-value for water *Phys. Med. Biol.* **54** 3451–72
Emfietzoglou D, Nikjoo H and Pathak A 2006 A comparative study of dielectric response function models for liquid water *Radiat. Prot. Dosim.* **122** 61–5
Fippel M and Soukup M 2004 A Monte Carlo dose calculation algorithm for proton therapy *Med. Phys.* **31** 2263–73
Friedland W, Dingfelder M, Kundrat P and Jacob P 2011 Track structures, DNA targets and radiation effects in the biophysical Monte Carlo simulation code PARTRAC *Mutat. Res.* **711** 28–40
Friedland W, Jacob P, Bernhardt P, Paretzke H G and Dingfelder M 2003 Simulation of DNA damage after proton irradiation *Radiat. Res.* **159** 401–10
Garcia-Molina R, Abril I, Denton C D, Heredia-Avalos S, Kyriakou I and Emfietzoglou D 2009 Calculated depth-dose distributions for H^+ and He^+ beams in liquid water *Nucl. Instrum. Methods* B **267** 2647–52
Garcia-Molina R, Abril I, Kyriakou I and Emfietzoglou D 2011 Energy loss of swift protons in liquid water: role of optical data input and extension algorithms *Radiation Damage in Biomolecular Systems* ed M Fuss and G Garcia (London: Canopus Academic) at press
Goitein M, Lomas A J and Pedroni E 2002 Treating cancer with protons *Phys. Today* **55** 45–51
González-Muñoz G, Tilly N, Fernández-Varea J M and Ahnesjö A 2008 Monte Carlo simulation and analysis of proton energy-deposition patterns in the Bragg peak *Phys. Med. Biol.* **53** 2857–75
Gudowska I, Sobolevsky N, Andreo P, Belkic D and Brahme A 2004 Ion beam transport in tissue-like media using the Monte Carlo code SHIELD-HIT *Phys. Med. Biol.* **49** 1933–58
Hayashi H, Watanabe N, Udagawa Y and Kao C C 2000 The complete optical spectrum of liquid water measured by inelastic x-ray scattering *Proc. Natl Acad. Sci. USA* **97** 6264–6
Heredia-Avalos S, Garcia-Molina R and Abril I 2007a Energy loss calculation of swift C_n^+ (n= 2–60) clusters through thin foils *Phys. Rev.* A **76** 012901
Heredia-Avalos S, Garcia-Molina R, Fernández-Varea J M and Abril I 2005 Calculated energy loss of swift He, Li, B, and N ions in SiO_2, Al_2O_3, and ZrO_2 *Phys. Rev.* A **72** 052902
ICRU 1993 Stopping Powers and Ranges for Protons and Alpha Particles *ICRU Report 49* (Bethesda, MD: ICRU)
Kiefer J 2008 The physical basis for the biological action of heavy ions *New J. Phys.* **10** 075004
Kraft G 2000 Tumor therapy with heavy charged particles *Prog. Part. Nucl. Phys.* **45** S473–544
Liamsuwan T, Uehara S, Emfietzoglou D and Nikjoo H 2011 Physical and biophysical properties of proton tracks of energies 1 keV to 300 MeV in water *Int. J. Radiat. Biol.* **87** 141–60
Lindborg L and Nikjoo H 2011 Microdosimetry and radiation quality determinations in radiation protection and radiation therapy *Radiat. Prot. Dosim.* **143** 402–8
Lindhard J 1954 On the properties of a gas of charged particles *Dan. Mat. Fys. Medd.* **28** no 8
Mermin N D 1970 Lindhard dielectric function in the relaxation-time approximation *Phys. Rev.* B **1** 2362–3
Meyer L 1971 Plural and multiple scattering of low-energy heavy particles in solids *Phys. Status Solidi* **b 44** 253–68

Möller W, Pospiech G and Schrieder G 1975 Multiple scattering calculations on ions passing through thin amorphous foils *Nucl. Instrum. Methods* **130** 265–70

Nastasi M, Mayer J W and Hirvonen J K 1996 *Ion–Solid Interactions: Fundamentals and Applications* (Cambridge: Cambridge University Press) chapter 5

Nikjoo H, Emfietzoglou D, Watanabe R and Uehara S 2008b Can Monte Carlo track structure codes reveal reaction mechanisms in DNA damage and improve radiation therapy? *Radiat. Phys. Chem.* **77** 1270–9

Nikjoo H, O'Neill P O, Wilson W E and Good head D T 2001 Computational approach for determining the spectrum of DNA damage induced by ionizing radiation *Radiat. Res.* **156** 577–83

Nikjoo H, Uehara S, Emfietzoglou D and Brahme A 2008a Heavy charged particles in radiation biology and biophysics *New J. Phys.* **10** 075006

Nikjoo H, Uehara S, Emfietzoglou D and Cucinotta F A 2006 Track-structure codes in radiation research *Radiat. Meas.* **41** 1052–74

Nikjoo H, Uehara S, Wilson W E, Hoshi M and Goodhead D T 1998 Track structure in radiation biology: theory and applications *Int. J. Radiat. Biol.* **73** 355–64

Obolensky O I, Surdutovich E, Pshenichnov I, Mishustin I, Solov'yov A V and Geiner W 2008 Ion beam cancer therapy: fundamental aspects of the problem *Nucl. Instrum. Methods* B **266** 1623–8

Olivera G H, Fainstein P D and Rivarola R D 1996 Contribution from the inner shell of water vapour to dose profiles under proton and alpha particle irradiation *Phys. Med. Biol.* **41** 1633–47

Paganetti H 2005 Interpretation of proton relative biological effectiveness using lesion induction, lesion repair, and cellular dose distribution *Med. Phys.* **32** 2548–56

Paganetti H and Kooy H 2010 Proton radiation in the management of localized cancer *Expert Rev. Med. Devices* **7** 275–85

Paganetti H, Niemierko A, Ancukiewicz M, Gerweck L E, Goitein M, Loeffler J S and Suit H D 2002 Relative biological effectiveness (RBE) values for proton beam therapy *Int. J. Radiat. Oncol. Biol. Phys.* **53** 407–21

Paul H 2010 Recent results in stopping power for positive ions, and some critical comments *Nucl. Instrum. Methods* B **268** 3421–5

Paul H, Geithner O and Jakel O 2007a The influence of stopping powers upon dosimetry for radiation therapy with energetic ions *Adv. Quantum Chem.* **52** 289–306

Paul H, Geithner O and Jakel O 2007b The ratio of stopping powers of water and air for dosimetry applications in tumor therapy *Nucl. Instrum. Methods* B **256** 561–4

Plante I and Cucinotta F A 2008 Ionization and excitation cross sections for the interaction of HZE particles in liquid water and application to Monte Carlo simulation of radiation tracks *New J. Phys.* **10** 125020

Podgoršak E B 2006 *Radiation Physics for Medical Physicist* (Berlin: Springer)

Press W H, Teukolsky S A, Vetterling W T and Flannery B P 1997 *Numerical Recipes in Fortran 77. The Art of Scientific Computing* 2nd edn (Cambridge: Cambridge University Press)

Ritchie R H 1957 Plasma losses by fast electrons in thin films *Phys. Rev.* **106** 874–81

Salvat F, Fernández-Varea J M and Sempau J 2003 PENELOPE—a code system for Monte Carlo simulation of electron and photon transport *Workshop Proc. Issy-les-Moulineaux, France (Nuclear Energy Agency)* pp 1–241

Sanche L 2005 Low energy electron-driven damage in biomolecules *Eur. Phys. J.* D **35** 367–90

Schardt D, Elsässer T and Schulz-Ertner D 2010 Heavy-ion tumor therapy: physical and radiobiological benefits *Rev. Mod. Phys.* **82** 383–425

Schiwietz G and Grande P L 2001 Improved charge-state formulas *Nucl. Instrum. Methods* B **175–177** 125–31

Scifoni E, Surdutovich E and Solov'yov A V 2010a Spectra of secondary electrons generated in water by energetic ions *Phys. Rev.* E **81** 021903

Scifoni E, Surdutovich E and Solov'yov A V 2010b Radial dose distribution from carbon ion incident on liquid water *Eur. Phys. J.* D **60** 115–9

Shimizu M, Hayakawa T, Kaneda M, Tsuchida H and Itoh A 2010 Stopping cross-sections of liquid water for 0.3–2.0 MeV protons *Vacuum* **84** 1002–4

Shimizu M, Kaneda M, Hayakawa T, Tsuchida H and Itoh A 2009 Stopping cross sections of liquid water for MeV energy protons *Nucl. Instrum. Methods* B **267** 2667–70

Sigmund P 2006 *Particle Penetration and Radiation Effects. General Aspects and Stopping of Swift Point Charges* (*Springer Series in Solid-State Sciences* vol 151) (Berlin: Springer)

Siiskonen T, Kettunen H, Peräjärvi K, Javanainen A, Rossi M, Trzaska W H, Turunen J and Virtanen A 2011 Energy loss measurement of protons in liquid water *Phys. Med. Biol.* **56** 2367–74

Smith A R 2006 Proton therapy *Phys. Med. Biol.* **51** R491–504

Solov'yov A V, Surdutovich E, Scifoni E, Mishustin I and Greiner W 2009 Physics of ion beam cancer therapy: a multiscale approach *Phys. Rev.* E **79** 011909

Sommerer F, Parodi K, Ferrari A, Poljanc K, Enghardt W and Aiginger H 2006 Investigating the accuracy of the FLUKA code for transport of therapeutic ion beams in matter *Phys. Med. Biol.* **51** 4385–98

Stankovskiy A, Kerhoas-Cavata S, Ferrand R, Nauraye C and Demarzi L 2009 Monte Carlo modelling of the treatment line of the Proton Therapy Center in Orsay *Phys. Med. Biol.* **54** 2377–94

Tan Z, Xia Y, Liu X and Zhao M 2010a Proton inelastic mean free path in amino acids and protein over the energy range of 0.05–10 MeV *Nucl. Instrum. Methods* B **268** 2606–10

Tan Z, Xia Y, Liu X and Zhao M 2010b Proton inelastic mean free path in a group of bioorganic compounds and water in 0.05–10 MeV range—including higher-order corrections *Nucl. Instrum. Methods* B **268** 2337–42

Turner J E, Wright H A and Hamm R N 1985 A Monte Carlo primer for health physicists *Health Phys.* **48** 717–33

Uehara S, Toburen L H and Nikjoo H 2001 Development of a Monte Carlo track structure code for low-energy protons in water *Int. J. Radiat. Biol.* **77** 139–54

Watanabe N, Hayashi H and Udagawa Y 1997 Bethe surface of liquid water determined by inelastic x-ray scattering spectroscopy and electron correlation effects *Bull. Chem. Soc. Japan.* **70** 719–26

Wenzel W A and Whaling W 1952 The stopping cross section of D_2O ice *Phys. Rev.* **87** 499–503

Zajfman D, Both G, Kanter E P and Vager Z 1990 Multiple scattering of MeV atomic and molecular ions traversing ultrathin films *Phys. Rev.* A **41** 2482–88

Ziegler J F, Biersak J P and Ziegler M D 2008 *SRIM. The Stopping and Range of Ions in Matter* (Chester, MD: SRIM Co.) www.srim.org